# A fibrous cellulose paste formulation to manufacture structural parts using 3D printing by extrusion

C. Thibaut, A. Denneulin, S. Rolland Du Roscoat, D. Beneventi, L. Orgeas, D. Chaussy

# A fibrous cellulose paste formulation to manufacture structural parts using 3D printing by extrusion

*C. Thibaut‡†, A. Denneulin‡, S. Rolland du Roscoat†, D. Beneventi‡, L. Orgéas† and, D. Chaussy‡**

‡Univ. Grenoble Alpes, CNRS, Grenoble INP[a], LGP2, F-38000 Grenoble, France

†Univ. Grenoble Alpes, CNRS, Grenoble INP[a], 3SR, F-38000 Grenoble, France

*corresponding author:

mail: didier.chaussy@grenoble-inp.fr

tel: +33 (0)4 76 82 69 08

address: 461, rue de la Papeterie, CS 10065, 38402 Saint-Martin-d'Hères Cedex - France

Abstract

An optimized paste based on short natural cellulose fibers combined with carboxymethyl cellulose at a high dry content (42 wt.%) was implemented as a bio-based material for 3D printing by extrusion. The homogeneous paste exhibited a pronounced thinning behavior and yield stress; it was extruded using a screw extrusion-based direct ink writing system and could easily flow through a small nozzle. The

[a] **Institute of Engineering Univ. Grenoble Alpes**

optimized formulation enabled accurate additive manufacturing of parts using a natural air-drying process with or without an ethanol bath. We characterized the anisotropic shrinkage that occurred during the drying of 3D printed parts and proposed a compensation method to account for it. The obtained results emphasized that cellulose had a strong potential to be used as a raw material for 3D printing of cheap, lightweight, robust, and recyclable parts.

**Keywords**: 3D printing; cellulose; extrusion; bio-based material

## 1. Introduction

Additive manufacturing, often referred as 3D printing, is regarded as a disruptive technology with many application fields, including the automotive industry, medical field, and leisure sector. This process of joining materials is used to fabricate objects from 3D model data, usually layer upon layer, as opposed to subtractive manufacturing methodologies. Additive manufacturing comprises a wide range of different technologies, as described by ASTM International (2012), each with their own advantages and drawbacks. In general, the additive manufacturing process offers new design opportunities for complex and lightweight designs, short manufacturing lead times, and simple design modifications (Huang, Liu, Mokasdar, & Hou, 2013). This technology is compatible with a broad range of materials, such as metals, polymers, ceramics, gels, food, and bio-based materials (Wohlers, Caffrey, & Campbell., 2016).

Cellulose in the form of fibers, which is the most abundant bio-based polymer on earth with excellent mechanical properties (Dufresne, 2013), may be a very promising candidate for producing cheap, lightweight, robust, and recyclable 3D structures by 3D printing: It may be used not just as an additive for mechanical reinforcement or as a rheological modifier, but also for many other applications, as discussed in a recent review on 3D printing cellulose and its derivatives (Dai et al., 2019). Indeed, up to now, the potential uses of cellulose as a bulk material for 3D printing have not been fully explored (Wang et al., 2018). Additive manufacturing with cellulose as the main building block has been reported

for three categories of additive manufacturing processes of the seven defined by ASTM International (2012): Binder jetting (Sachs, Cima, Williams, Brancazio, & Cornie, 1992), sheet lamination (Feygin & Hsieh, 1991) and, material extrusion (US5121329A, 1992). This last process is promising because it allows the manufacture of complex and light parts with more than one material, unlike the binder jetting and sheet lamination processes. Thermoplastic polylactic acid (PLA), which is derived from starch, has been considered as a material reference for this study regarding the 3D printing material extrusion process due to its easy processing and extensive use (Steinle, 2016; Wittbrodt & Pearce, 2015).

It was only twenty years after the development of this 3D printing extrusion process, that cellulose was used for the first time to 3D print part by this process (based on our knowledge, Markstedt, Sundberg, & Gatenholm, 2014). It comes from the various challenges raised by the properties of cellulose and of this process. Unlike thermoplastic materials, which are compatible with 3D printing by melt extrusion, cellulose cannot be melted to be processed and so recover its stiffness when cool down. Thus, a solvent must be added to precisely control the filament extrusion during the forming step and to achieve higher accuracy of the 3D printed parts. The successful extrusion of a filament has three requirements: (i) a constant extrusion flow must be set which does not cause nozzle clogging or filament breaking under a constant pressure, (ii) the filament produced must have a homogeneous composition with a constant diameter, and (iii) the pressure required to force the material through the nozzle must be within the capabilities of the equipment used. After printing, the part must stand upright. Thus, the viscosity of the material should be sufficiently high. Finally, the part generally needs to be dried depending on the intended use and final properties. Quantitative indicators to assess the printability and shape fidelity of 3D printed part with a new developed formulation area current area of study (Wang et al., 2018).

Recently, several articles have been published on formulations compatible with 3D printing by extrusion with cellulose as the main building block. Herein, we are interested in formulations that can

achieve high-definition printing with nozzle diameters around 500 µm, and thus, formulations that require large nozzles are not presented (Sanandiya, Vijay, Dimopoulou, Dritsas, & Fernandez, 2018). These formulations can be divided into two groups: dissolved cellulose and cellulose suspensions.

*Dissolved cellulose:* Markstedt, Sundberg, & Gatenholm, 2014 used cellulose fibers dissolved in an ionic liquid (EmimAc (1-ethyl-3-methylimidazolium acetate)). One limitation was the solid content of their solutions (4 wt.%), which limited the pressure for the extrusion to 6 bars for their operating parameters (12.7 mm long needle with an inner diameter of 0.41 mm at a flow rate of 10 µL/min). Subsequently, they had to balance the rate of coagulation. If the coagulation occurred too quickly, there was poor adhesion between printed layers. However, if the coagulation occurred too slowly, there was a height limitation of the printed part to avoid its collapse L. Li, Zhu, & Yang, (2018) dissolved cellulose fibers in N-nethylmorpholine N-oxide (NMMO) at less than 10 wt.%. Their solution was printed at 70 °C and solidified after the extrusion, similar to the fused filament fabrication (FFF) method. Parts were successfully printed with heights around 1 cm. The printed part was freeze-dried to maintain the interconnected porous structures in the final product. Pattinson & Hart, 2017 used cellulose acetate at 25-30 wt.% in acetone. The quasi-immediate evaporation of the acetone (~1 min) during the printing allowed (i) the hardening of the part as it was printed and, (ii) the shrinkage compensation of every printed layer to maintain dimensional stability of the part. The main drawback of this approach was the speed limitation due to the acetone evaporation process.

*Suspension of cellulose:* Cellulose in its nanostructured form was dispersed in water with or without chemical modifications and, in some cases, with the addition of alginate at a very low concentration (<5 wt.%) (Chinga-Carrasco et al., 2018; Håkansson et al., 2016; V. C. F. Li, Mulyadi, Dunn, Deng, & Qi, 2018; Markstedt et al., 2015; Rees et al., 2015; Sultan & Mathew, 2018) and at larger concentration (around 20 wt.%) (Jia et al., 2017; Klar, Kärki, Orelma, & Kuosmanen, 2017; V. C.-F. Li, Dunn, Zhang, Deng, & Qi, 2017; Siqueira et al., 2017). The suspensions were successfully extruded through small nozzles and

deposited on a substrate to form parts of about 1 $cm^3$ with height from 0.2mm up to 30 mm to demonstrate the printability of the suspensions. Due the small sizes of the printed parts in most studies, these previous reports cannot assess (i) the absence of clogging issues due to nanocellulose aggregation in the nozzle nor (ii) the height limitations due to viscosities that are too small to resist the weight of the parts. Compared to acetone, the water evaporation rate at ambient conditions is low. Yet, the hardening and main deformation begins after completion of the 3D printed part. In general, these printed parts were used either in their wet states after cross-linking with solutions, such as $CaCl_2$ solutions, or were freeze-dried to produce porous media and preserve the 3D structure of the printed part. Håkansson et al., 2016 evaluated three other drying techniques less expensive than freeze drying for preserving the 3D structure and dimensions of printed parts with 2 wt.% nanocellulose suspensions in water: solvent exchange, addition of surfactant and air drying. Solvent exchange or addition of surfactant, which added a post-treatment step, only preserved the 3D structures of the parts whereas the air-drying technique did not preserve the 3D structure and dimensions. However, with a high-concentration nanocellulose suspension (22 wt.%), Klar, Kärki, Orelma, & Kuosmanen, 2017 successfully preserved the 3D structures and obtained an 80% volume shrinkage (i.e. around 5% porosity) after natural air drying. This large amount of shrinkage prevented compensation methods from being used. To compensate for the shrinkage, the volume of the 3D model part should be multiplied by five, which strongly impacts the printing time. Moreover, this printing time might be larger than the drying time of the first layers for large parts, causing shrinkage to begin before printing is complete, which can lead to printing failure.

These developed formulations with cellulose as the main component raised several questions: Can cellulose be a new, cheap, lightweight, robust, renewable, and biodegradable material compatible for 3D printing by extrusion similar to PLA? What form of cellulose (natural cellulose fiber, nanocellulose, cellulose derivative) should be used and with which solvent? What proportion of cellulose fibers is required to limit deformation after drying and the cost of the drying process while being an extrudable

material? Are there any design restrictions or new design opportunities compared to fused filament fabrication processes with thermoplastic materials, such as the bio-based PLA?

Herein, we report a new formulation based on natural cellulose fibers and a cellulose derivative that is compatible with extrusion-based 3D printing and a natural air-drying process with or without a solvent exchange step with ethanol. This formulation and process resulted in limited and anisotropic deformation that allowed the use of a compensation strategy. This new formulation easily flowed through the small nozzle and exhibited suitable specific mechanical properties after drying. We successfully printed complex parts and compensated for height deformation due to drying to maintain fidelity with the initial 3D digital model. The obtained printed parts were compared to parts obtained with PLA, the benchmark for 3D printing by extrusion of bio-based materials.

## 2. Experimental procedure

### 2.1 Material and paste preparation

A cellulose-based paste was prepared by dry mixing natural cellulose fibers and carboxymethyl cellulose (CMC) and adding distilled water.

- The cellulose fibers (Carl Roth) consisted of a mix of milled hardwood and softwood natural fibers, as illustrated in Figure 1A. The fiber length and width distributions were measured using the Morfi® approach (Techpap®, Grenoble, France) (Passas, R., Voillot, C., Tarrajat, G., Khélifi, B., & Tourtollet, G., 2001). Figure 1B and C show that (i) 90% of the fibers were shorter than 200 µm and (ii) fibers longer than 100 µm had a mean fiber width of 27 µm, respectively.

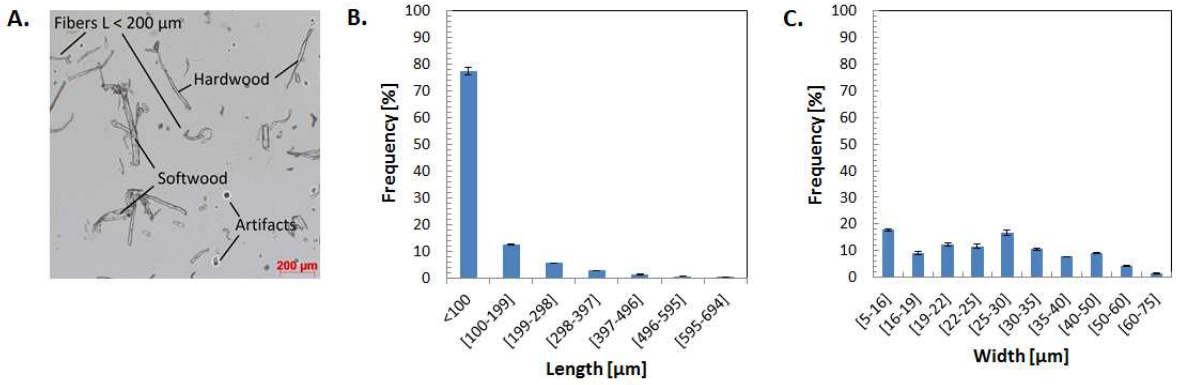


Figure 1. Optical characterization of cellulose fibers. (A) Image of natural cellulose fibers in suspension. (B) Length distribution of cellulose fibers. (C) Width distribution of cellulose fibers with lengths greater than 100 µm.

- Sodium CMC with an average molecular weight of 90,000 and 0.7 carboxymethyl groups per anhydroglucose unit was purchased from Sigma Aldrich.

Batches of 100 g of the cellulosic paste were prepared with a CMC/fiber mass ratio ranging from 0.13 to 1.33, after which distilled water was added to adjust the dry solid contents. The paste was homogenized for 5 min at 120 rpm using a planetary mixer (Proline RP10). The paste was stored for 24 h in a refrigerator at 4–5 °C before printing.

The formulations had overall dry contents varying from 35 to 50 wt.%, cellulose fiber contents varying from 15 to 45 wt.%, and CMC contents varying from 5 to 20 wt.%. These ratios were chosen after preliminary testing to achieve a balance between the extrusion processes of the paste, increase the solid content in the cellulose fibers to limit the shrinkage upon drying, and increase the CMC content to promote fiber dispersion by increasing the viscosity of the distilled water.

### 2.2 3D printing by extrusion

*Printer:* A commercial 3D printer Prusa i3 was upgraded with a liquid deposit modeling (LDM) WASP extruder (Figure 2.A). An air pressure syringe (caption 1 of Figure 2A) was used to feed the cavity of the LDM extruder with the paste described in Section 2.1. This cavity was placed in the device just before the paste entered the LDM extruder. The extruder consisted of a screw-driven device (2) in a barrel (3) and a steel nozzle (4) with an outlet diameter *d* varying from 0.5 to 0.9 mm. The inner shapes of the nozzles were designed with two successive constrictions from a diameter of approximately 5 mm to the final outlet diameter *d*. This device could apply up to 40 bar of pressure to the paste, a significantly higher pressure than the typical 7 bar pressures achieved by pneumatic extruders. This LDM extruder allowed the use of highly viscous pastes at printing speeds of the same order of magnitude as those of the FFF process, ranging from 10 to 50 mm $s^{-1}$. It was possible to quickly interrupt the flow by changing the direction of the screw rotation to release the pressure applied to the paste. To compensate for the pressure loss due to the nozzle, the rotational velocity of the screw was set 2 to 3 times larger than the pressure used when the nozzle was absent to achieve the flow required for accurate 3D printing. The rotation velocity of the screw was approximately 10 rpm during printing.

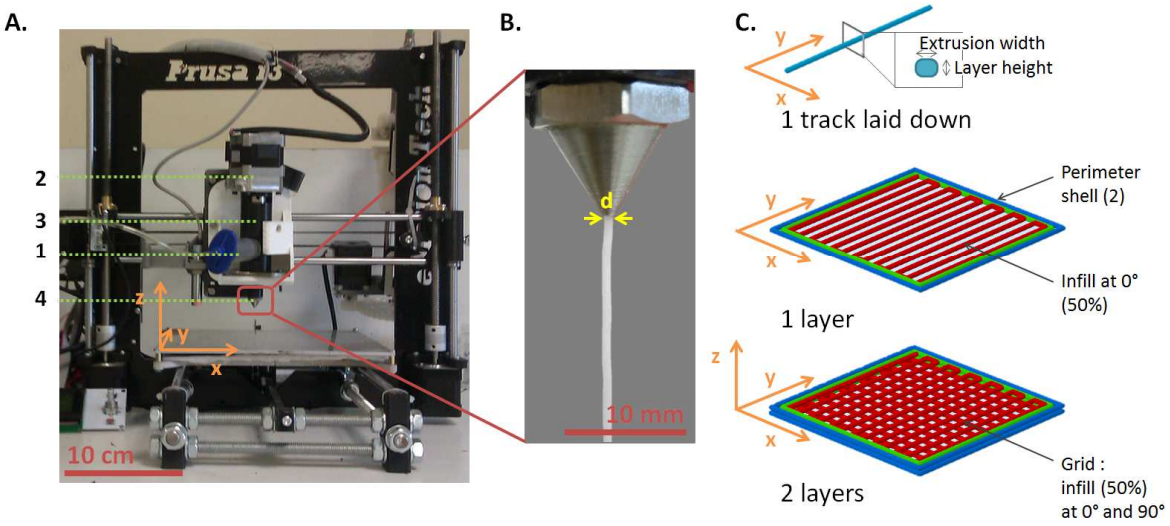


163

164 Figure 2. (A) 3D printer Prusa i3 upgraded with a Liquid Deposit Modeling WASP Extruder. (1) Air
165 pressure syringe, (2) screw-driven device, (3) barrel, and (4) steel nozzle. (B) Close-up of nozzle with an
166 inner diameter of 0.7 mm. Smooth filaments could be extruded without apparent swelling. (C)
167 Visualization obtained using Simplify 3D of one track, one layer, and two layers of a cube

168

169 *Printed parts:* In general, to 3D print a part, a CAD model is first sliced orthogonally in the z direction
170 in thin layers, which are then divided into tracks by a slicing software (Simplify 3D in this study) using
171 several key parameters: (i) the extrusion width (thickness of the track laid down), (ii) the layer height
172 (thickness of each layer), (iii) the infill (density of rectilinear pattern in one layer), and (iv) the perimeter
173 shell (solid wall of the model). These parameters are illustrated in Figure 2C. This dataset and the
174 printing speed are converted to a programming language compatible with the printer. One layer at a
175 time, the extruder head (and/or the build platform on which the part is manufactured) moves in the
176 (x,y) plane and extrudes material shaped as a flatten filament in order to create one cross-section of the
177 part. After completing the layer, the extruder head lifts (or the building plate lowers) to the height of a
178 layer thickness to build the next layer of the part on top of the previous layer, and this process continues
179 until the part is completed. Various geometrical parts (2D and 3D) were printed using the upgraded

printer and pastes described in Section 2.1. First, single filaments of 100 and 200 mm were extruded using a 0.7 mm diameter nozzle at a linear flow ranging from 3 to 5 mm $s^{-1}$ at approximately 20 cm above the printing surface. Figure 2B shows the typical filaments obtained. Five different geometric models with increasing complexity were tested: (i) a 6 $cm^3$ cube; (ii) a 4.0 cm high monofilament rectangular cuboid with a 4.00 $cm^2$ square cross-section; (iii) a 1.5 cm long bridge with a 1 cm high pillar and rectangular cross-section of 0.5 × 1.0 $cm^2$; (iv) a 3DBenchy model composed of complex 3D printing shapes, including a 40° overhang, 1.0–2.0 cm bridge, and 1 cm high narrow pillar with a 0.15 $cm^2$ cross-section; and (v) a 5.0 cm high double spiral vase with an opening diameter of 1.6 cm. Models (iv) and (v) were downloaded from the Thingiverse database (Thingiverse.com, March 2018). The printing parameters are given in Table 1.

| **3D model name** | **Cube** | **Monofilament rectangular cuboid** | | **Bridge** | **3DBenchy** | **Double spiral vase** |
|---|---|---|---|---|---|---|
| **Nozzle diameter [mm]** | 0.7 | 0.7 | 0.9 | 0.5 | 0.5 | 0.5 |
| **Extrusion width [mm]** | 0.7 | 0.7 | 0.9 | 0.5 | 0.5 | 0.5 |
| **Layer height [mm]** | 0.56 | 0.56 | 0.70 | 0.40 | 0.30 | 0.30 |
| **Printing speed [mm $s^{-1}$]** | 10 | 10 | | 10 | 20 | 15 |
| **Infill [%]** | 50 | 0 | | 100 | 50 | 100 |
| **Perimeter shell** | 2 | 1 | | 2 | 2 | 2 |

**Table 1.** 3D printing parameters

*Drying:* Once printed, the samples (filament and 3D parts) were dried using two different methods. They were either (i) conditioned at 23 °C and 50% relative humidity for 48 h or (ii) immersed in an ethanol (95%) bath for 2 h (30 min for extruded filament) to exchange the solvent with a lower surface tension solvent, as reported by Håkansson et al., 2016, followed by conditioning (as described in (i)).

During the drying process, the filament was suspended from the support for at least 30 min to avoid friction. The length of this filament was short enough to prevent it from stretching under its own weight.

*Dimension measurements:* After drying, the dimensions of the printed filaments and 3D parts were measured. To measure the filament diameters, three images per filament were taken with a binocular magnifier at ×100 (ZEISS SteREO Discovery V20 with an AxioCam ICc 5) with a pixel size of 0.54 µm, two centimeters apart all along the filament length. The obtained pictures were analyzed using the imageJ "Analyze stripes v2.4.5.b" plugin (Copyright 2013 Justin R. Bickford) to measure the distance between the edges of the filament, which was considered to be the filament diameter. The filament length was measured with a graduated ruler (± 0.05 cm). The height of the monofilament cuboid was measured with a digital caliper (± 0.01 mm) at the four edges of the cuboid and at four central points between two consecutive edges to obtain the mean value and standard deviation. The height and outlet diameter of the dried double spiral vase were measured with the same digital caliper. The areas of the holes of the 50% infilled 6 $cm^3$ cube were measured on the undried region: (i) an image of the 6 $cm^3$ cube just after completion of the printing (<5 min) was taken with the binocular magnifier at ×7.5 with a pixel size of 7 µm and (ii) the dark holes of the grid were counted and their area measured using imageJ. Measurements were performed on 56 holes.

*Weight measurement:* After the filaments were dried and their dimensions were measured, three filaments were stored for 48 h in a conditioned room at 23 ℃ and 50% RH, after which they were weighed to within ± 0.0001 g.

## 2.3 Characterization

### 2.3.1 Rheology of the pastes

To characterize the rheology of the cellulosic pastes in the "fresh" state, *i.e.*, at the nozzle exit, we performed lubricated squeeze flow tests using a universal tension-compression testing machine equipped with a 2 kN load cell (Instron 5944). These tests are well-suited to study the rheology of highly viscous pastes reinforced with fibers of finite lengths. Indeed, characterizing the rheology of such (fiber-reinforced) pastes using standard shear or high pressure capillarity rheometers may be difficult due to (i) the size of fibers (Chalencon et al., 2010; Orgéas, Dumont, Le, & Favier, 2008) and (ii) their marked shear thinning, which often causes to undesirable wall slippage and shear banding (Martoïa et al., 2015) (Orgéas, Gabathuler, Imwinkelried, Paradies, & Rappaz, 2003). We prepared cylindrical samples from the pastes with initial heights $h_0$ = 7 mm and diameters $d_0$ = 10 mm. Each sample was placed between two parallel compression plates that were lubricated with thin layers of a mixture of silicon oil and grease to ensure a homogeneous compression flow of the sample. The samples were monitored with a video camera. The recorded videos showed that samples flowed at nearly constant volume (less than 2% of volume variation of the cylinder at the end of the tests). Using the compression force $F$ measurements and the actual sample height $h$, we plotted the evolution of the compression Cauchy stress, $|\sigma| = 4|F|h/\pi h_0 d_0^2$, with time $t$ and with the compression Hencky strain, $|\varepsilon| = |\ln h/ h_0|$. The tests were first carried out at constant compression velocity $\dot{h}$ and with initial compression strain rates $|\dot{\varepsilon}_0|$ ranging from 0.01 to 1 $s^{-1}$, up to a compression strain $|\varepsilon| = 0.8$. Subsequently, the compression ended and the stress relaxation was recorded for 2 mins, *i.e.*, up to steady-state regimes with approximately constant stresses. Three samples were used for each testing condition, and the error bars given in the following graphs correspond to the min and max values recorded during these tests.

### 2.3.2 Deformation after drying

The deformation was calculated as the absolute value of the engineering strain $|e|=|X_{dried}/X_{fresh}-1|$, where $X_{dried}$ corresponds to the measurements obtained using the methods described in the *Dimension*

*measurements* section in Section 2.2 and $X_{fresh}$ corresponds to (i) the dimensions given in the *Printed part* section in Section 2.2 or (ii) the nozzle diameter for transversal strain of the filament, as no apparent swelling was observed. The longitudinal and transversal strains of the filament diameter were calculated for each formulation on three air dried 10.0 ± 0.2 cm long filaments extruded through the 0.7 mm diameter nozzle at an output flow of 3 mm $s^{-1}$. The strain of the 4 cm high monofilament cuboid was calculated for each formulation with two air dried samples. The strain of the vase was calculated on a single sample.

### 2.3.3 SEM observations

To characterize the microstructures of the extruded filaments, two types of samples were recorded: (i) filaments dried with or without an ethanol bath with cross-sections cut using a razor blade with an angle of approximately 45° and (ii) air dried filaments after the tensile tests. Samples cut with the razor blade were metalized with a thin layer of gold and palladium (around 1 nm) and the tensile tested sample was metalized with carbon. Then, SEM images of the surface and cross-section of the filament were recorded on a FEI Quanta 200.

### 2.3.4 Tensile test

To characterize the mechanical properties of the paste after drying, we performed tensile tests with a universal tension-compression testing machine (Instron 5965) equipped with a 5 kN load cell in a conditioned room (23 °C, 50% RH). We prepared filament samples that were extruded through a 0.7 mm diameter nozzle at an output flow of 4.5 mm $s^{-1}$ and dried with or without solvent exchange in ethanol. The initial diameters of the dried samples were measured by an image analysis (Section 2.2 *Dimension measurements,* measurement of filament diameter) with a 10 cm gage length. As discussed in Section 2.3.1, we plotted the Cauchy stress as a function of the Hencky strain, which can be approximated from the engineering strain for small deformations. The tests were carried out at a

constant stretch velocity of 10 mm $min^{-1}$ until filament breakage. Five samples were measured for each drying condition.

## 3. Results and discussion

### 3.1 Optimization of the formulation of the cellulose-based paste for 3D printing by extrusion

To identify an optimized cellulose-based paste formulation compatible with 3D printing by extrusion, several pastes with varying solid contents and proportions of compounds were evaluated.

A.

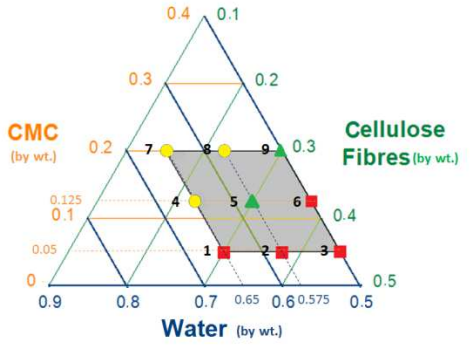


B.

| Caption | Monofilament cuboid (20*20*40 mm³) | N° Formulation | Cuboid height → deformation | Diameter of filament → deformation | Length of filament → deformation |
|---|---|---|---|---|---|
| Not compatible with 3D printing by extrusion |  Not completed | 1 | - | - | - |
| | | 2 | - | - | - |
| | | 3 | - | - | - |
| | | 6 | - | - | - |
| Partially compatible with 3D printing by extrusion |  | 4 | 24±1 mm → 41±2% | 0.48±0.04 mm → 34±5% | 91±1 mm → 9±2% |
| | | 7 | 23±1 mm → 43±3% | 0.44±0.02 mm → 38±3% | 95±1 mm → 5±2% |
| | | 8 | 25±1 mm → 39±3% | 0.48±0.02 mm → 33±3% | 95±1 mm → 5±2% |
| Compatible with 3D printing by extrusion |  | 5 | 26±1 mm → 34±3% | 0.51±0.01 mm → 30±1% | 97±1 mm → 3±2% |
| | | 9 | 27±1 mm → 32±4% | 0.53±0.01 mm → 27±2% | 97±1 mm → 3±2% |

Figure 3. (A) Ternary diagram indicating the weight fractions of CMC, cellulose fibers, and water for the tested formulations. (B) Qualitative and quantitative characterization of the nine different tested formulations for compatibility with 3D printing by extrusion.

Figure 3A shows the compositions of the nine tested formulations. These formulations were assessed according three main criteria, which ensured the accuracy of the printed part relative to the 3D model: (i) extrusion of an adequate filament, as defined in the Introduction; (ii) production of undried and accurate 3D printing parts that do not collapse; and (iii) limiting and forecasting the deformation after drying. These criteria were applied to a 10 cm long filament and the monofilament cuboid part that was extruded, printed, and air dried using the parameters specified in Section 2.2 and in Table 1.

Figure 3B shows the typical results obtained with the nine tested formulation, which were as follows:

- The tested formulations with cellulose fiber contents of 37.5 wt.% or with a CMC content at 5 wt.% did not allow the extrusion of smooth and regular filaments with a nozzle diameter of 0.7 mm, as the extruded filaments were friable and irregular, which led to filament breakage. Furthermore, these characteristics did not allow the complete printing of a regular monofilament wall cuboid, as can be seen in Figure 3B. These formulations were found to be incompatible with 3D printing by extrusion, as they did not meet criteria (i) based on filament extrusion, and (ii) based on the accuracy of the undried 3D printed part.
- The five remaining tested formulations with cellulose fiber contents of 30 wt.% or less and a CMC content of 12.5 wt.% or more yielded smooth and regular filaments extruded through a 0.7 mm diameter nozzle, allowing the manufacture of a monofilament cuboid as high as 4 cm with a wall thickness of the size of the nozzle outlet, as no die swelling was observed. These parts did not collapse under their own weights, as can be seen in Figure 3B. Indeed, the lower region of the 3D part did not widen. However, the stacked extruded filaments were not perfectly aligned. This misalignment might be due to a small amount of over-extrusion or a small displacement of the corner caused by the motion of the nozzle and the extruded paste that generates imperfections or the buckling of the thin walls under the pressure caused by the extruded paste (Buswell, Leal de Silva, Jones, & Dirrenberger, 2018; Suiker, 2018). These five formulations were found to be compatible with 3D printing by extrusion to manufacture wet parts, as they met criteria (i) based on adequate filament extrusion, and (ii) based on the accuracy of the undried 3D printed part.
- Figure 3B also summarizes the strain of the extruded filament and the height of the cuboid after drying. For formulations with a cellulose fiber content lower than 30 wt.%, the strains of the filaments were larger than 30% and 5% for the diameters and lengths, respectively, and the height strain of the cuboid was larger than 35%. Therefore, these formulations with cellulose fiber

contents lower than 30 wt.% were found to be partially compatible with 3D printing by extrusion because of the high strain observed after drying (criteria (iii)). By comparison, the formulations containing 30 wt.% of cellulose fibers and CMC contents of 12.5% or 20 wt.% exhibited better strain behaviors during the drying phase. These two last formulations were found to be compatible with 3D printing by extrusion, as they fulfilled criteria (i) based on adequate filament extrusion, (ii) based on the accuracy of the undried 3D printed part and, and (iii) based on limitation of the deformation after drying.

To conclude, the formulation with a dry content of 42.5 wt.%, a cellulose fiber content of 30 wt.%, and a CMC content of 12.5 wt.% was selected as the optimized formulation, because its cost was lower than a similar formulation in which 7.5 wt.% of distilled water was replaced by CMC, and because the paste that was formed was easily processed, facilitating simple filling of the syringe (Appendix 1). This optimized formulation was equivalent to a solid content of 23.3 vol.% based on the cellulose fiber density of 1.5 g $cm^{-3}$ in a CMC gel at 0.22 g $mL^{-1}$. This cellulose fiber solid content was two times lower than the solid content used in the other two pastes successfully formulated for 3D printing by extrusion at ambient temperature with a nozzle diameter smaller than 500 µm: (i) 45 vol.% of glass powder with up to 2 wt.% of CMC (Eqtesadi et al., 2013) and (ii) 47 vol.% of lead zirconate titanate and a cellulose concentration of 5 mg $mL^{-1}$ (Smay, Cesarano, & Lewis, 2002). This difference in solid content might arise from the components used. The glass powder and lead zirconate titanate were unlike cellulose fibers, as they had smaller dimensions (< 10 µm), round geometries, and low interactions with water (e.g. hydrogen bonding or hygroexpansion). Using an elongated cellulose mat, V. C. F. Li et al., 2018 and Siqueira et al., 2017 also successfully formulated a paste at high solid content with 20 wt.% of freeze-dried cellulose nanocrystals (CNCs) as received or modified CNC in suspension. They limited their solid content to 20 wt.% owing to limitations of the devices used for mixing and/or printing, which did not allow proper homogenization of the paste or sufficient extrusion flow or alignment of the CNCs. These

solid contents were lower than the optimized formulation (30 wt.% of cellulose fibers) proposed herein. These differences were due to the use of a screw-driven device instead of a pneumatic device and the addition of CMC, which reduced the friction between fibers.

### 3.2 Characterization of the optimized formulation

In the following section, we discuss the properties of the optimized paste.

#### 3.2.1 Rheological behavior of the fresh paste

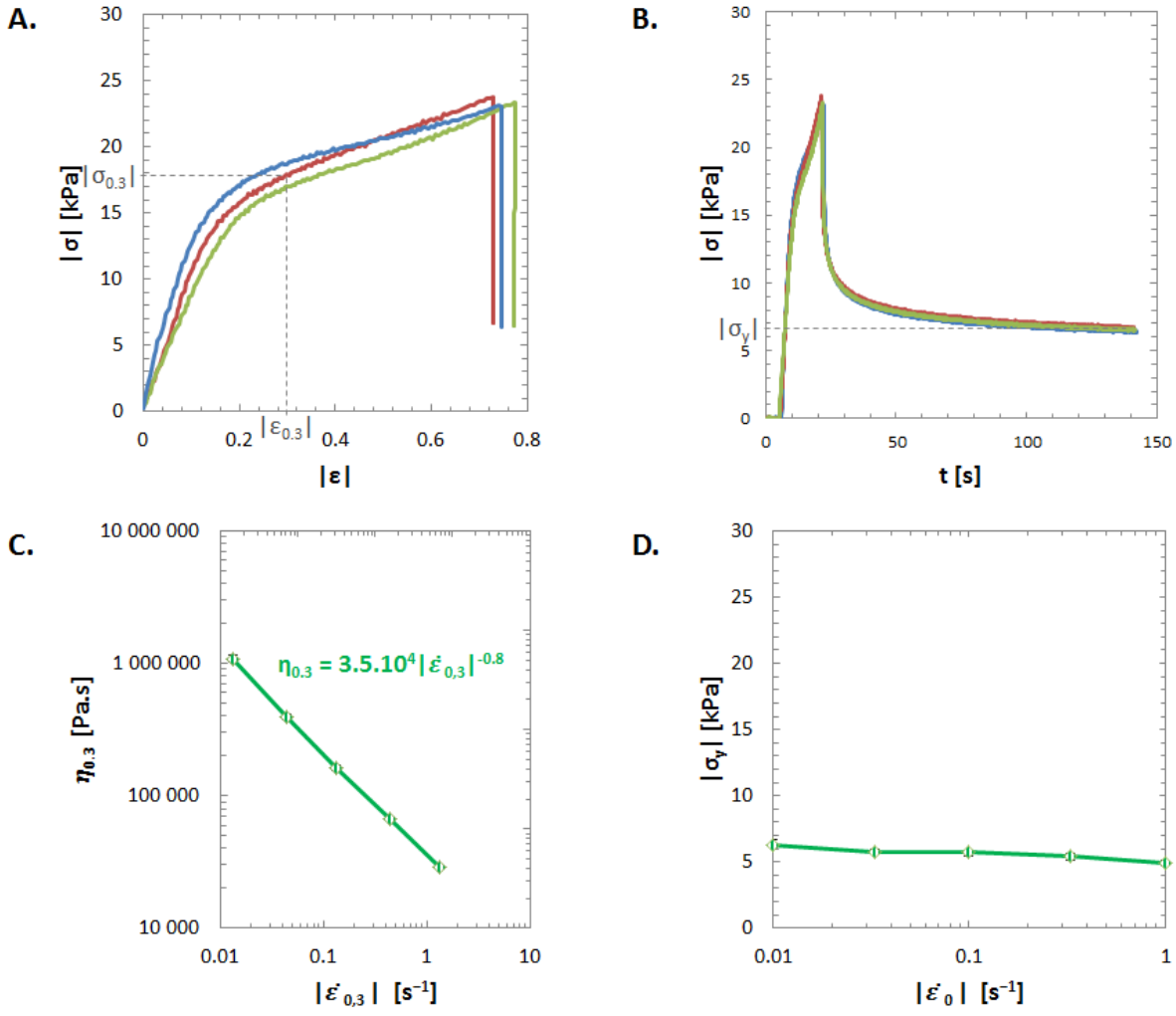


Figure 4. Rheological properties of the optimized formulation (30 wt.% cellulose fiber, 12.5 wt.% carboxymethyl cellulose, 57.5 wt.% distilled water). Three lubricated squeeze flow tests (compression at

constant speed followed by 2 min of relaxation) were performed at an initial compression strain rate of 0.033 $s^{-1}$. (A) Stress-strain curves. (B) Stress during the lubricated squeeze flow test. During the relaxation time, the stress reached a plateau, which corresponds to the yield stress $|\sigma_y|$. (C) Viscosity curve fit with a power law, $\eta_{0.3} = k|\dot{\varepsilon}_0|^{n-1}$. (D) Yield stress $|\sigma_y|$= 6 kPa as a function of the initial strain rate.

Figure 4A and B show typical stress-strain and stress-time curves recorded with the optimized formulation during three compression tests, which were obtained at a first compression flow of 3.33 $10^{-2}$ $s^{-1}$. Similar curves were obtained for the formulation listed as compatible in Figure 3B. High reproducibility of the stresses was observed, with deviations of less than ± 10%. After a quasi-linear and sharp increase of the stresses, the samples flowed more easily, exhibiting stress hardening behaviors that are typical of fiber-reinforced paste materials (Chalencon et al., 2010; Orgéas et al., 2008).

We arbitrarily characterized the transition between these two regimes using the compression stress $|\sigma_{0.3}|$ recorded at a compression strain $|\varepsilon|$ = 0.3. As shown in Figure 4C, the compression viscosity $\eta_{0.3}$ = $\sigma_{0.3}/\dot{\varepsilon}_{0.3}$ decreased with the strain rate $|\dot{\varepsilon}_{0.3}|$ and followed a power-law function, *i.e.*, $\eta_{0.3} = k|\dot{\varepsilon}_{0.3}|^{n-1}$. The value obtained for the power-law exponent, $n$ = 0.2, indicates the optimized pastes exhibited a pronounced thinning behavior, which is similar to those obtained for similar fiber-reinforced paste materials. The stress levels recorded here one order of magnitude higher than those reported under shear for other 3D printing formulations (Compton & Lewis, 2014; Lewis, 2006; Siqueira et al., 2017; Smay et al., 2002).

When the compression flow stopped, the compression stress rapidly decreased to reach a steady and constant stress (Figure 4B), which corresponds to the yield stress $|\sigma_y|$ after the paste flow. Figure 4D shows that $|\sigma_y|$ achieved finite values that were independent of the initial strain rate $|\dot{\varepsilon}_0|$ (Figure 4D). The yield stress $|\sigma_y|$, which was measured for the "fresh" state, is one of the most critical parameters for 3D printing from a mechanical standpoint (as the paste liquid phase evaporates, the yield stress is

362 expected to increase). If the stress state in a “fresh” printed filament remains below the yield stress, the
363 filament should behave as an elastic solid and maintain its printed shape. Above this value of yield
364 strength, the dimensional stability may be lost, as the paste can flow.

365 **3.2.2 Shrinkage during drying**

366 As illustrated in Figure 3B, after drying, the filament diameter and length decreased. The filament
367 diameter decreased from 0.72 to 0.49 ± 0.1 mm, and its length decreased from 200 to 193 mm. The
368 strain was primarily radial. These dimensional changes were due to the 57.5 wt.% of distilled water in
369 the optimized paste. During the drying phase, the water must evaporate. During this process, water is
370 transported from the inside to the outside of the printed part, leading to high drying stresses, such as
371 the capillarity pressure (Scherer, 1990). The capillary forces tend to bring the cellulose fibers embedded
372 in dissolved CMC closer together (i.e. mainly in their longitudinal direction), resulting in strain.
373 Moreover, the hygroexpansion of a cellulose fiber is larger in the transversal direction than in the
374 longitudinal direction: over the relative humidity range from 0% to 100% at 23 °C, a single cellulose fiber
375 roughly expanded by 1% in the longitudinal direction, whereas it expanded about 20 to 30% in the radial
376 direction (Wainwright, Biggs, & Currey, 1982). Thus, the strain of filament is mainly a radial strain, which
377 suggests that most of the cellulose fibers were aligned in the extrusion flow direction, as shown in Figure
378 5.

379 Figure 5B and D show SEM images of the inner structure of a filament dried with or without ethanol,
380 respectively. In both cases, a porous phase was present. This suggests that the deformation ends before
381 the end of the drying phase. Thus, the stiffness of the partially dried paste was sufficient to resist the
382 drying forces. Moreover, the characteristics of the porous phase were dependent of the drying process.
383 More pores were observed on the cross-section of the dried filament with ethanol exchange than on the
384 cross-section of the air-dried filament. This produced a larger diameter for the filament with the ethanol
385 bath, as is shown in Figure 5A and C. Indeed, the diameter of the dried filament with ethanol exchange

decreased from 0.72 to 0.56 ± 0.2 mm, whereas the dried filament without ethanol exchange decreased from 0.72 to 0.49 ± 0.1 mm for the same set of extruded filaments. This improvement is a consequence of the lower surface tension of ethanol compared to that of water (22 vs 72 mN $m^{-1}$, respectively) resulting in a capillary pressure that was three times lower during the drying phase. This resulted in a lower density for the filament with ethanol exchange after drying: 0.8 (with ethanol exchange) vs 1.1 (without ethanol exchange) $g.cm^{-3}$.

### 3.2.3 Microstructure of the extruded filament

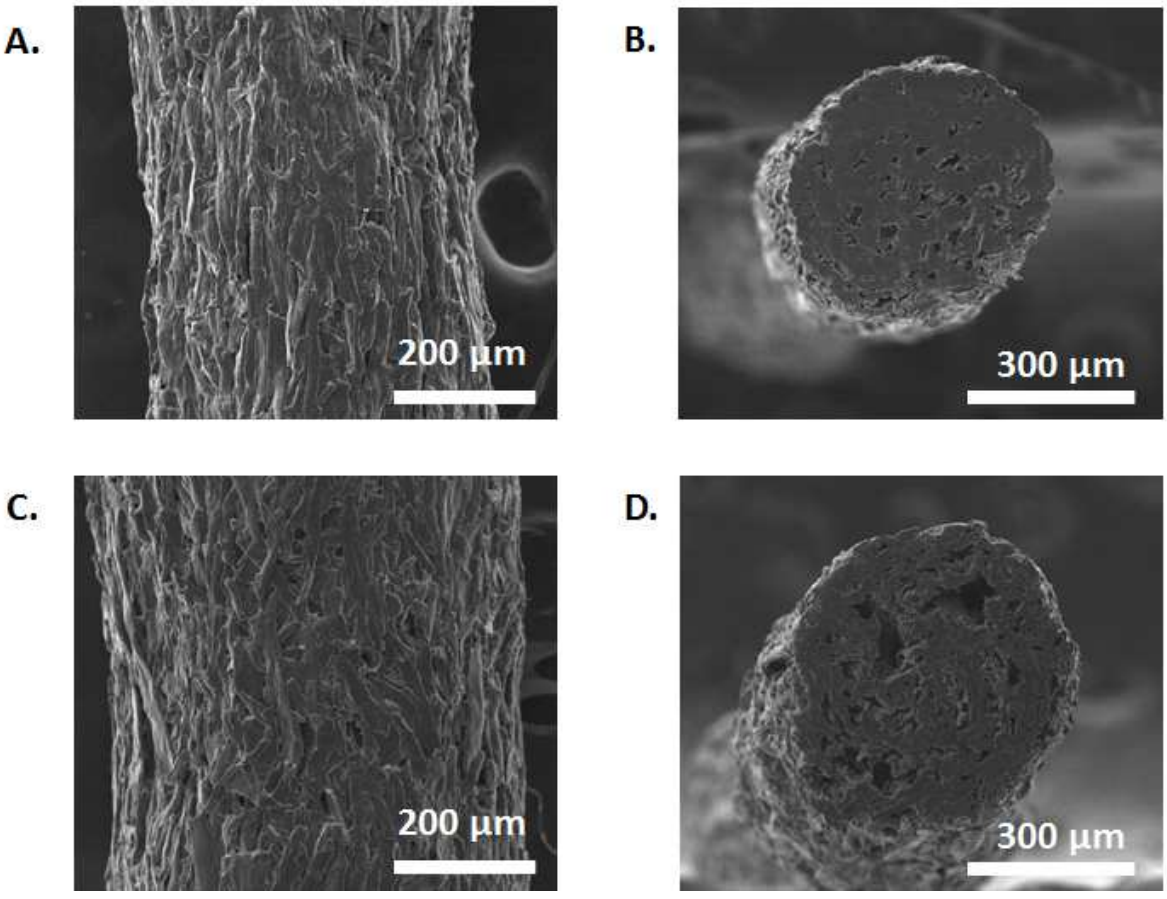


Figure 5. SEM images of the surface and cross-section of an (A, B) air dried filament and (C, D) air dried filament with ethanol exchange.

As shown in Figure 5A and C, the cellulosic fibers were mainly aligned in the extrusion direction, independent of the drying technique used. These alignments may have been enhanced by the capillary forces during the drying process.

The filament cross-sections are shown in Figures 5B and D, showing homogeneous solid phases where only the cross section of the cellulosic fibers can be seen. The characteristics of the porous phase were dependent on the drying process.

These last observations confirmed the following: (i) The initial paste was homogeneous due to the mixing process that kept the cellulose fibers dispersed in this gelatinous matrix, forming a single phase paste. (ii) The flow through the 0.7 mm nozzle was homogeneous, as no fiber aggregation or detachment was observed, despite a mean cellulose fiber width of 27 µm for cellulose fibers with lengths larger than 100 µm. This may have been owing to the CMC. Indeed, the addition of CMC dissolved in water in the formulation acted as a gelation agent by increasing the water viscosity (Edali, Esmail, & Vatistas, 2001) and allowed the cellulose fibers to be embedded, which reduced the friction between fibers. (iii) High stresses developed in the nozzle due to the elongational strain and shear rate caused by the successive constrictions inside the nozzle and its small outlet diameter. For instance, the apparent shear rate value was $10^{1}$–$10^{2}$ $s^{-1}$ for a flow rate of 5mm $s^{-1}$ through nozzles with outlet diameters of 0.5–0.7 mm. These high stresses might be the main factor that induced fiber alignment.

### 3.2.4 Tensile properties of the filament

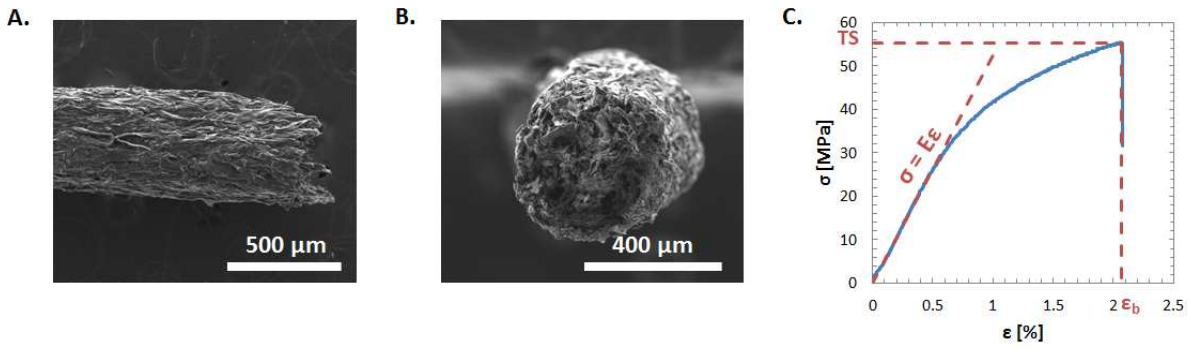


Figure 6. SEM images of a fractured air dried filament extruded through a 0.7 mm nozzle diameter: (A) surface and (B) cross-section. (C) Typical stress-strain curve obtained for a tested air-dried filament.

Figure 6A and B show the fractured surfaces in the rupture zone of an air-dried filament after the tensile test. The cross-section of the filament after fracture was not sharp as those shown in Figure 5, indicating that some fibers broke away from the surrounding fibers. The strain stress curve obtained from the tensile test of a dried filament shown in Figure 6C is typical of the behavior of a brittle material without a strain-hardening region. From this strain-stress curve, the Young's modulus can be determined. For the air-dried filament, the Young's modulus was 5.4±0.5 GPa, whereas the Young's modulus of the ethanol exchange dried filament was two times lower, with a value of 2.7±0.3 GPa. This difference in stiffness was partially due to the higher porosity (42%) of the air dried filament with the ethanol bath compared to that (30%) of the air dried one without the ethanol bath, as illustrated in Figure 5B and D and calculated from their densities. However, such a difference in the Young's moduli cannot only be explained by the difference in porosities and presence of defects below the image resolution. Indeed, if we consider that the ethanol exchange dried filament had the same diameter as the air dried filament, the Young's modulus was about 3.5±0.5 GPa, which is still lower than the 5.4±0.5 GPa of the air dried filament. Thus, the ethanol does not only affect the strain during drying, but it also might influence the hydrogen bonding between the cellulose fibers (Przybysz, Dubowik, Kucner, Przybysz, & Buzała, 2016) or the CMC-cellulose fiber adhesion.

The Young's moduli of the dried filaments were of the same order of magnitude as tensile test specimens of PLA using the Fused Filament Fabrication process, which range from 2 to 3 GPa according to the PLA data sheet of Stratasys, Ltd. This reinforces the hypothesis that this new cellulosic paste is compatible with the market expectations.

### 3.3 3D model printability

#### 3.3.1 Fresh model

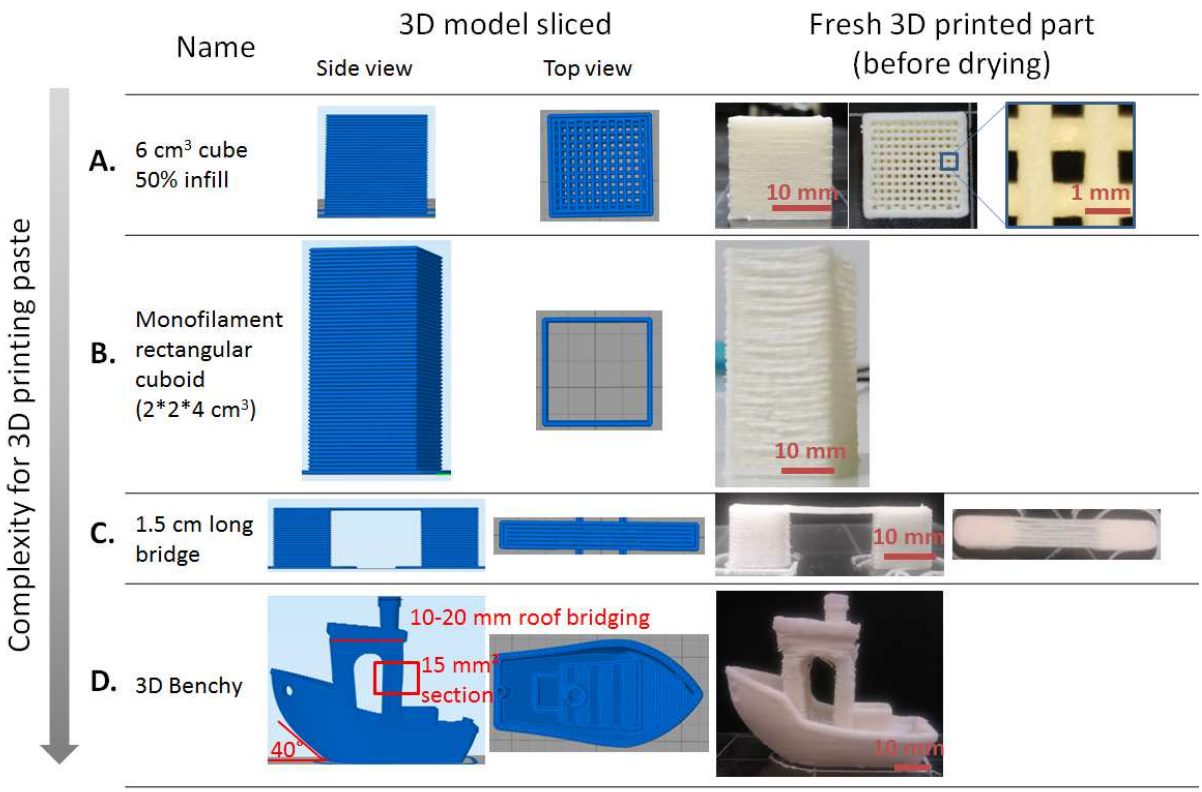


Figure 7. 3D parts in order of increasing 3D printing complexity from (A) a cube to (D) the 3DBenchy. The side and top views of each 3D model slice and the corresponding printed cellulose part after completion are presented.

Figure 7 illustrates the 3D sliced models and fresh 3D printed part corresponding to the printing parameters presented in Table 1 using the optimized formulation. First, we fully succeeded in printing a

6 $cm^3$ cube with 50% filling and two perimeter shells using a nozzle with a diameter of 0.7 mm (Figure 7A). The double perimeter wall of the printed cube appeared straight, and the inner grid was well defined with a 6% standard deviation of the hole sizes. The successfully printed monofilament wall cuboid, which was presented earlier, is shown again in Figure 7B. While there was a low contact surface area (58 $mm^2$) between the build platform and the first layer, there was a good adhesion during printing whereas for the FFF printing of thermoplastics, care must be taken to obtain a good adhesion (such as the temperature of the build platform) (Spoerk, Gonzalez-Gutierrez, Sapkota, Schuschnigg, & Holzer, 2018). A more complex 3D model was implemented to characterize the bridging capacity of the paste. Figure 7C shows a successfully printed 15 mm long bridge. The success in printing this part was in one hand due to the paste characteristics, such as restoring its strength just after exiting the nozzle. The bridge remained straight after printing because the stress levels in the fresh state were below $|\sigma_y|$. Using the Euler-Bernoulli beam theory and assuming that the filament behaves as a straight beam clamped at its extremities under its own weight, the maximal tension-compression stresses in the filament (located at its extremities) is $|\sigma_{max}| = 2\rho g L_f^2/3d_f \approx 3.4$ kPa, which is below the value of 6 kPa given in Figure 4D. The successful printing of this part was also due to the extrusion flow rate adjustment. A flow rate that is too large will cause sagging of the suspended part of the bridge, whereas a flow rate that is too small will result in filament breaking. For the most complex model, the 3DBenchy (Figure 7.D), which took about 1 h to print, the 40° overhang using a nozzle diameter of 0.5 mm, and a layer height of 0.3 mm (i.e. 50% of the width of the unsupported filament), exhibited no apparent defects. However, the four 10 cm high pillars with smaller sections (<15 $mm^2$) were not printed well. Indeed, the pillars were flexible and moved with the printing head, resulting in crooked pillars. Unlike thermoplastics that become rigid upon cooling, the paste used herein requires drying to become stiffer to resist rapid motion of the nozzle on small surfaces. The bridging between the flexible pillars required several layers (~5) to stiffen the structure and allow printing without defects.

### 3.3.2 Model after drying

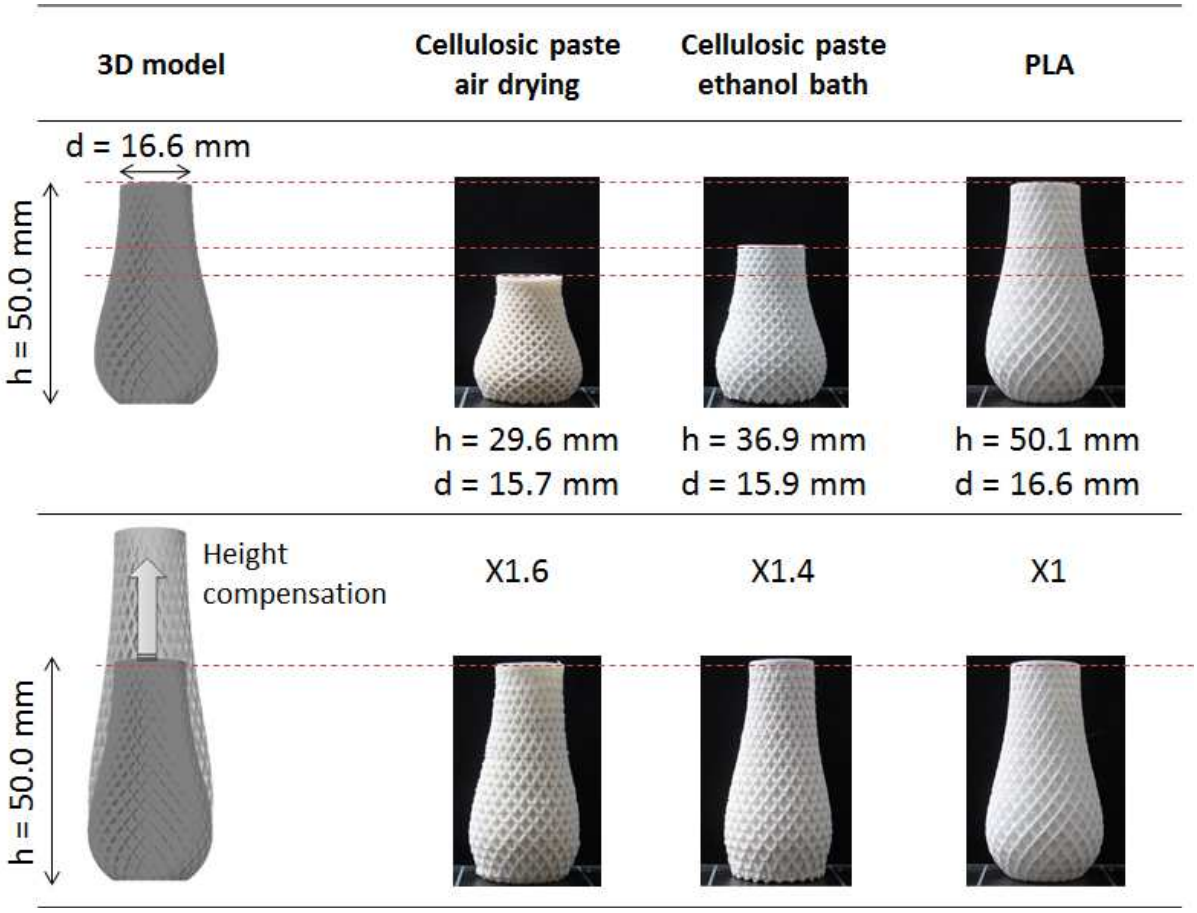


Figure 8. 3D printing of a double spiral vase with the optimized formulation dried with or without an ethanol bath or with polylactic acid (PLA). Upper row: 50 mm high vase. Lower row: vase with height compensation in the model based on the calculated strain.

Figure 8 shows 3D printed solid vases with the optimized paste or with polylactic acid (PLA). The vases in the first row of Figure 8 were printed with the same 3D model. As expected, the vase printed with PLA maintained shape fidelity, as it did not exhibit any dimensional variations from the model. When printed

with the optimized paste, the air-dried model exhibited height and external diameter outlet strains of 41% and 5%, respectively. These strains decreased to 26% and 4%, respectively, by the addition of an ethanol bath before air drying. The height strain of the vase was larger than the radial strain measured on a single filament (c.f. Section 3.2.2). This may have been due to (i) the subsidence of the first layers due to an overhang of 45° with almost 60% of the filaments unsupported, (ii) the addition of a load during drying due the weight of the layers pressing down on the lower layer, and (iii) a larger drying time due to a smaller surface contact and greater volume compared to those of a filament. The strain of the external diameter outlet was a combination of length and radial strains of the filament. These strains, mainly observed in the vertical plan of the part, enable us to devise a strategy to directly compensate for the height change by introducing a height compensation in the digital 3D model to obtain a printed and solid (dried) part with the desired height. The results are shown in Figure 8. With a multiplier coefficient of 1.6, a printed vase similar to the one produced using fused filament fabrication with PLA was achieved. This multiplier coefficient in height on the digital model was slightly lower than the calculated strain for the 50 mm high vase (-5%). This may be due to (i) no subsidence of the first layer of the 80 mm high vase due to a lower overhang of 32° and (ii) a compensation of the height strain due to slow drying during the printing (printing time x~1.6). However, this compensation approach becomes less practical for printing larger objects. Therefore, the solvent exchange (water-> ethanol), which minimized the radial strain of the filament, may be a good option for reducing dimension changes upon drying. Indeed, the 3D printed 50 mm high vase immersed in ethanol after completion showed a significantly lower strain, with only 26% height strain compared to the 41% strain for the non-immersed part. In this case, a multiplier coefficient of 1.4 was used to compensate for the drying strain (Figure 8).

## 4. Conclusion

In this work, an innovative bio-based material for 3D printing by extrusion with a low-cost drying solution was developed. A formulation with a high solid content was optimized based on specific criteria to ensure accuracy between the cellulose printed part and the 3D model: (i) filament extrusion, (ii) manufacturing accuracy, and (iii) limiting and forecasting deformation after drying. We proposed a paste with a cellulose fiber content of 30 wt.%, a CMC content of 12.5 wt.%, and 57.5 wt.% of distilled water. This paste exhibited a pronounced thinning behavior and a yield stress after relaxation, which are critical parameters for 3D printing parts. Moreover, homogeneous filaments that exhibited high Young's moduli (~5 GPa) in a dry state were produced by a screw-driven device with nozzle diameters ranging from 0.9 to 0.5 mm. This allowed the 3D printing of complex geometries. Design limitations linked to the printing of tall and thin elements, such as the 10 mm high pillar with a cross-section of 15 $mm^2$, were identified. A strategy to limit the isotropic deformation during air drying was proposed by adding a water-to-ethanol exchange step after printing the fresh part. This decreased the shrinkage by one third from 36% to 24% on average and divided the Young's modulus by two. These results emphasized that cellulose has a strong potential to be used as a material for 3D printing with the promise of producing cheap, lightweight, robust, and recyclable parts.

## Acknowledgements

This work was supported by the Idex UGA grant (AGIR). The LGP2 and 3SR laboratories are part of the LabEx Tec 21 (Investissements d'Avenir: grant agreement no. ANR-11-LABX-0030) and the PolyNat Carnot Institute (Investissements d'Avenir: grant agreement no. ANR-16-CARN-0025-01). This research was possible owing to the facilities of the TekLiCell platform funded by the Région Rhône-Alpes (ERDF: European Regional Development Fund).

## References

ASTM International. (2012). *Standard terminology for additive manufacturing technologies: designation F2792-12a*. West Conshohocken, PA: ASTM International.

Buswell, R. A., Leal de Silva, W. R., Jones, S. Z., & Dirrenberger, J. (2018). 3D printing using concrete extrusion: A roadmap for research. *Cement and Concrete Research*, *112*, 37–49. https://doi.org/10.1016/j.cemconres.2018.05.006

Chalencon, F., Orgéas, L., Dumont, P. J. J., Foray, G., Cavaillé, J.-Y., Maire, E., & Rolland du Roscoat, S. (2010). Lubricated compression and X-ray microtomography to analyse the rheology of a fibre-reinforced mortar. *Rheologica Acta*, *49*(3), 221–235. https://doi.org/10.1007/s00397-009-0393-5

Chinga-Carrasco, G., Ehman, N. V., Pettersson, J., Vallejos, M. E., Brodin, M. W., Felissia, F. E., … Area, M. C. (2018). Pulping and pretreatment affect the characteristics of bagasse inks for three-dimensional printing. *ACS Sustainable Chemistry & Engineering*, *6*(3), 4068–4075. https://doi.org/10.1021/acssuschemeng.7b04440

Compton, B. G., & Lewis, J. A. (2014). 3D-printing of lightweight cellular composites. *Advanced Materials (Deerfield Beach, Fla.)*, *26*(34), 5930–5935. https://doi.org/10.1002/adma.201401804

Crump, S. S. (1992). *US5121329A*. United States. Retrieved from https://patents.google.com/patent/US5121329/en

Dai, L., Cheng, T., Duan, C., Zhao, W., Zhang, W., Zou, X., … Ni, Y. (2019). 3D printing using plant-derived cellulose and its derivatives: A review. *Carbohydrate Polymers*, *203*, 71–86. https://doi.org/10.1016/j.carbpol.2018.09.027

Dufresne, A. (2013). *Nanocellulose: From nature to high performance tailored materials*. Walter de Gruyter.

549 Edali, M., Esmail, M. N., & Vatistas, G. H. (2001). Rheological properties of high concentrations of
550 carboxymethyl cellulose solutions. *Journal of Applied Polymer Science*, *79*(10), 1787–1801.
551 https://doi.org/10.1002/1097-4628(20010307)79:10<1787::AID-APP70>3.0.CO;2-2
552 Eqtesadi, S., Motealleh, A., Miranda, P., Lemos, A., Rebelo, A., & Ferreira, J. M. F. (2013). A simple recipe
553 for direct writing complex 45S5 Bioglass® 3D scaffolds. *Materials Letters*, *93*, 68–71.
554 https://doi.org/10.1016/j.matlet.2012.11.043
555 Feygin, M., & Hsieh, B. (1991). Laminated Object Manufacturing (LOM): a simpler process.
556 https://doi.org/10.15781/T2PV6BQ54
557 Håkansson, K. M. O., Henriksson, I. C., de la Peña Vázquez, C., Kuzmenko, V., Markstedt, K., Enoksson, P.,
558 & Gatenholm, P. (2016). Solidification of 3D printed nanofibril hydrogels into functional 3D
559 cellulose structures. *Advanced Materials Technologies*, *1*(7), n/a-n/a.
560 https://doi.org/10.1002/admt.201600096
561 Huang, S. H., Liu, P., Mokasdar, A., & Hou, L. (2013). Additive manufacturing and its societal impact: a
562 literature review. *The International Journal of Advanced Manufacturing Technology*, *67*(5),
563 1191–1203. https://doi.org/10.1007/s00170-012-4558-5
564 Jia, C., Bian, H., Gao, T., Jiang, F., Kierzewski, I. M., Wang, Y., … Hu, L. (2017). Thermally stable cellulose
565 nanocrystals toward high-performance 2D and 3D nanostructures. *ACS Applied Materials &*
566 *Interfaces*, *9*(34), 28922–28929. https://doi.org/10.1021/acsami.7b08760
567 Klar, V., Kärki, P., Orelma, H., & Kuosmanen, P. (2017). Analysis of drying deformation of 3D printed
568 nanocellulose structures. In *Cellulose Materials Doctoral Students Conference 2017*. Graz
569 University of Technology, TUG. Retrieved from
570 https://research.aalto.fi/en/publications/analysis-of-drying-deformation-of-3d-printed-
571 nanocellulose-structures(447440d2-bf95-47bb-98ab-f9984beb3f4a).html

572 Lewis, J. A. (2006). Direct ink writing of 3D functional materials. *Advanced Functional Materials*, *16*(17),
573 2193–2204. https://doi.org/10.1002/adfm.200600434
574 Li, L., Zhu, Y., & Yang, J. (2018). 3D bioprinting of cellulose with controlled porous structures from
575 NMMO. *Materials Letters*, *210*, 136–138. https://doi.org/10.1016/j.matlet.2017.09.015
576 Li, V. C. F., Mulyadi, A., Dunn, C. K., Deng, Y., & Qi, H. J. (2018). Direct ink write 3D printed cellulose
577 nanofiber aerogel structures with highly deformable, shape recoverable, and functionalizable
578 properties. *ACS Sustainable Chemistry & Engineering*, *6*(2), 2011–2022.
579 https://doi.org/10.1021/acssuschemeng.7b03439
580 Li, V. C. F., Dunn, C. K., Zhang, Z., Deng, Y., & Qi, H. J. (2017). Direct Ink Write (DIW) 3D printed cellulose
581 nanocrystal aerogel structures. *Scientific Reports*, *7*(1), 8018. https://doi.org/10.1038/s41598-
582 017-07771-y
583 Markstedt, K., Mantas, A., Tournier, I., Martínez Ávila, H., Hägg, D., & Gatenholm, P. (2015). 3D
584 bioprinting human chondrocytes with nanocellulose-alginate bioink for cartilage tissue
585 engineering applications. *Biomacromolecules*, *16*(5), 1489–1496.
586 https://doi.org/10.1021/acs.biomac.5b00188
587 Markstedt, K., Sundberg, J., & Gatenholm, P. (2014). 3D bioprinting of cellulose structures from an ionic
588 liquid. *3D Printing and Additive Manufacturing*, *1*(3), 115–121.
589 https://doi.org/10.1089/3dp.2014.0004
590 Martoïa, F., Perge, C., Dumont, P. J. J., Orgéas, L., Fardin, M. A., Manneville, S., & Belgacem, M. N.
591 (2015). Heterogeneous flow kinematics of cellulose nanofibril suspensions under shear. *Soft*
592 *Matter*, *11*(24), 4742–4755. https://doi.org/10.1039/c5sm00530b
593 Nguyen, D., Hägg, D. A., Forsman, A., Ekholm, J., Nimkingratana, P., Brantsing, C., … Simonsson, S.
594 (2017). Cartilage tissue engineering by the 3D bioprinting of iPS cells in a nanocellulose/Alginate
595 Bioink. *Scientific Reports*, *7*(1), 658. https://doi.org/10.1038/s41598-017-00690-y

596 Orgéas, L., Gabathuler, J.-P., Imwinkelried, T., Paradies, C., & Rappaz, M. (2003). Modelling of semi-solid
597 processing using a modified temperature-dependent power-law model. *Modelling and*
598 *Simulation in Materials Science and Engineering*, *11*(4), 553. https://doi.org/10.1088/0965-
599 0393/11/4/309
600 Orgéas, L., Dumont, P. J. J., Le, T.-H., & Favier, D. (2008). Lubricated compression of BMC, a concentrated
601 and fibre-reinforced granular polymer suspension. *Rheologica Acta*, *47*(5), 677.
602 https://doi.org/10.1007/s00397-008-0276-1
603 Passas, R., Voillot, C., Tarrajat, G., Khélifi, B., Pétot, E. & Tourtollet, G. (2001). MorFi : analyseur
604 morphologique des fibres. (2001),SFGP
605 Pattinson Sebastian W., & Hart A. John. (2017). Additive manufacturing of cellulosic materials with
606 robust mechanics and antimicrobial functionality. *Advanced Materials Technologies*, *2*(4),
607 1600084. https://doi.org/10.1002/admt.201600084
608 Przybysz, P., Dubowik, M., Kucner, M. A., Przybysz, K., & Buzała, K. P. (2016). Contribution of hydrogen
609 bonds to paper strength properties. *PLOS ONE*, *11*(5), e0155809.
610 https://doi.org/10.1371/journal.pone.0155809
611 Rees, A., Powell, L. C., Chinga-Carrasco, G., Gethin, D. T., Syverud, K., Hill, K. E., & Thomas, D. W. (2015).
612 3D bioprinting of carboxymethylated-periodate oxidized nanocellulose constructs for wound
613 dressing applications. https://doi.org/10.1155/2015/925757
614 Sachs, E., Cima, M., Williams, P., Brancazio, D., & Cornie, J. (1992). Three dimensional printing: rapid
615 tooling and prototypes directly from a CAD model. *Journal of Engineering for Industry*, *114*(4),
616 481–488. https://doi.org/10.1115/1.2900701
617 Sanandiya, N. D., Vijay, Y., Dimopoulou, M., Dritsas, S., & Fernandez, J. G. (2018). Large-scale additive
618 manufacturing with bioinspired cellulosic materials. *Scientific Reports*, *8*(1), 8642.
619 https://doi.org/10.1038/s41598-018-26985-2

620 Scherer, G. W. (1990). Theory of drying. *Journal of the American Ceramic Society*, *73*(1), 3–14.
621 https://doi.org/10.1111/j.1151-2916.1990.tb05082.x
622 Siqueira, G., Kokkinis, D., Libanori, R., Hausmann, M. K., Gladman, A. S., Neels, A., Studart, A. R. (2017).
623 Cellulose nanocrystal inks for 3D printing of textured cellular architectures. *Advanced Functional*
624 *Materials*, *27*(12), n/a-n/a. https://doi.org/10.1002/adfm.201604619
625 Smay, J. E., Cesarano, J., & Lewis, J. A. (2002). Colloidal inks for directed assembly of 3-D periodic
626 structures. *Langmuir*, *18*(14), 5429–5437. https://doi.org/10.1021/la0257135
627 Spoerk, M., Gonzalez-Gutierrez, J., Sapkota, J., Schuschnigg, S., & Holzer, C. (2018). Effect of the printing
628 bed temperature on the adhesion of parts produced by fused filament fabrication. *Plastics,*
629 *Rubber and Composites*, *47*(1), 17–24. https://doi.org/10.1080/14658011.2017.1399531
630 Steinle, P. (2016). Characterization of emissions from a desktop 3D printer and indoor air measurements
631 in office settings. *Journal of Occupational and Environmental Hygiene*, *13*(2), 121–132.
632 https://doi.org/10.1080/15459624.2015.1091957
633 Suiker, A. S. J. (2018). Mechanical performance of wall structures in 3D printing processes: Theory,
634 design tools and experiments. *International Journal of Mechanical Sciences*, *137*, 145–170.
635 https://doi.org/10.1016/j.ijmecsci.2018.01.010
636 Sultan, S., & Mathew, A. P. (2018). 3D printed scaffolds with gradient porosity based on a cellulose
637 nanocrystal hydrogel. *Nanoscale*, *10*(9), 4421–4431. https://doi.org/10.1039/c7nr08966j
638 Thingiverse.com. (n.d.). Thingiverse - Digital Designs for Physical Objects. Retrieved March 13, 2018,
639 from https://www.thingiverse.com/
640 Wainwright, S. A., Biggs, W. D., & Currey, J. D. (1982). *Mechanical design in organisms*. Princeton
641 University Press.
642 Wang, Q., Sun, J., Yao, Q., Ji, C., Liu, J., & Zhu, Q. (2018). 3D printing with cellulose materials. *Cellulose*,
643 *25*(8), 4275–4301. https://doi.org/10.1007/s10570-018-1888-y

644 Wittbrodt, B., & Pearce, J. M. (2015). The effects of PLA color on material properties of 3-D printed
645 components. *Additive Manufacturing*, *8*, 110–116.
646 https://doi.org/10.1016/j.addma.2015.09.006
647 Wohlers, T. , Caffrey, T. &, Campbell, I. (2016). *Wohlers report 2016: 3D printing and additive*
648 *manufacturing state of the industry : Annual Worldwide Progress Report*. Wohlers Associates.
649